

Flexible Alignment Super-Resolution Network for Multi-Contrast MRI

Yiming Liu¹, Member, IEEE, Mengxi Zhang¹, Weiqin Zhang,
Bo Hou, Dan Liu, Heqing Lian, Member, IEEE, Bo Jiang

Abstract—Magnetic resonance images play an essential role in clinical diagnosis by acquiring the structural information of biological tissue. However, during acquiring magnetic resonance images, patients have to endure physical and psychological discomfort, including irritating noise and acute anxiety. To make the patient feel cozier, technically, it will reduce the retention time that patients stay in the strong magnetic field at the expense of image quality. Therefore, Super-Resolution plays a crucial role in preprocessing the low-resolution images for more precise medical analysis. In this paper, we propose the Flexible Alignment Super-Resolution Network (FASR-Net) for multi-contrast magnetic resonance images Super-Resolution. The core of multi-contrast SR is to match the patches of low-resolution and reference images. However, the inappropriate foreground scale and patch size of multi-contrast MRI sometimes lead to the mismatch of patches. To tackle this problem, the Flexible Alignment module is proposed to endow receptive fields with flexibility. Flexible Alignment module contains two parts: (1) The Single-Multi Pyramid Alignment module serves for low-resolution and reference image with different scale. (2) The Multi-Multi Pyramid Alignment module serves for low-resolution and reference image with the same scale. Extensive experiments on the IXI and FastMRI datasets demonstrate that the FASR-Net outperforms the existing state-of-the-art approaches. In addition, by comparing the reconstructed images with the counterparts obtained by the existing algorithms, our method could retain more textural details by leveraging multi-contrast images.

Index Terms—Magnetic resonance imaging, Multi-Contrast Super-Resolution, feature fusion, feature alignment.

I. INTRODUCTION

MAGNETIC Resonance Imaging (MRI) is a non-invasive imaging modality that enables the observation of three-dimensional detailed anatomical images. The basic principle of MRI is placing the human body in a powerful magnetic

This work was supported by the National Science Fund for Distinguished Young Scholars under Grant 81601485. (Yiming Liu and Mengxi Zhang contributed equally to this work. Corresponding authors: Heqing Lian; Bo Jiang.)

Yiming Liu and Heqing Lian are with the Xiao Ying AI Lab, Beijing, China. (liyiming@xiaoyingai.com, lianheqing@xiaoyingai.com).

Mengxi Zhang is with the School of Electrical and Information Engineering, Tianjin University, Tianjin, China. (mengxizhang@tju.edu.cn).

Weiqin Zhang is with the School of Artificial Intelligence, University of Chinese Academy of Sciences, Beijing, China. (zhang-weiqin21@mailsucas.ac.cn)

Bo Jiang, Dan Liu and Bo Hou are with Peking Union Medical College Hospital, Beijing, China. (jbpumch@163.com, liud2104@163.com, mailto:houbobo97@pumch.cn)

field to align hydrogen nuclei in the body. Subsequently, radio frequency current stimulates hydrogen nuclei in the human body, causing the hydrogen nuclei to resonate and absorb energy. After the radio frequency field is turned off, the hydrogen nuclei emit radio signals at a specific frequency and release the absorbed energy. Thus, the MRI sensors can detect the energy released as the hydrogen nuclei realign with the magnetic field.

Magnetic Resonance Imaging (MRI) plays a significant role in providing clear information about soft tissue structure. Compared with other modalities, such as nuclear imaging and computed tomography (CT), MRI has the distinct advantage of not requiring ionizing radiation. However, due to the complex data acquisition process and long repetition time, obtaining high-resolution (HR) MRI means high system cost-effectiveness. Patients must keep stable in narrow space and endure irritating noise when acquiring MRI. These may lead to uncomfortable performances of patients, such as inevitable motion, which will shrink image quality.

Super-Resolution reconstruction technology can improve the image quality without changing the hardware settings, which extensively utilized as the post-processing tool to overcome the difficulty in obtaining HR MRI scans [1], [2]. The research on image SR is divided into two categories: single-image Super-Resolution (SISR) and reference-based image Super-Resolution (Ref-SR). SISR only adopts a single low-resolution (LR) image to recover HR images, which highly depends on the prior knowledge of training sets. Some transformer-based methods achieve fantastic results in SISR, such as [3], [4]. In case of domain shift between training sets and test sets, the complementary details are inferred by training sets. As a result, SISR often produces blurry effects because the HR textural features cannot be effectively recovered in the reconstruction process. The texture information of medical images is crucial evidence for doctors' diagnoses. Therefore, SISR is not suitable for the medical image Super-Resolution.

Ref-SR adopts an additional high-resolution reference image as an auxiliary, which transfers HR textures and details to the LR image in the process of SR. In clinical settings, MRI generates multi-contrast images for diagnosis together. Due to different settings, the appearances and functions of these images are widely divergent. However, these images are used as complementary information for diagnosing the same anatomical structure. Generally, T1, T2, PD, and FS-PD weighted images are produced together in the acquisition

of MRI. Clinically, T1 weighted images have shorter repetition and echo time than T2 weighted images, while PD-weighted images usually take faster than FS-PD weighted images in the scanning process [5]. Inspired by this, we propose a MRI Ref-SR approach to recover textures and details more accurately.

The most crucial step of Ref-SR is the feature fusion [6] between LR and Ref images, aiming at transferring the helpful detailed information from Ref to LR images. This operation is similar to feature fusion of video frames and the left and right viewing angle in Binocular Stereo Vision. Some researches roughly combine Ref and LR feature maps through the plus or concatenation operation, which limit the improvement of the LR images quality. Subsequently, a series of methods adopt deformable convolution and cross-attention mechanism [7], [8], [9]. These methods have verified that the positional information, which means matching valuable information of Ref images to the corresponding position of LR images, strongly impacts the reconstruction of HR images. We call this process image alignment. EDVR [7] introduces deformable convolution to align the input images. Cross-attention mechanism is also adopted to enhance the image quality.

Existing state-of-the-art (SOTA) feature fusion methods usually utilize Transformer-based cross-attention mechanism [8], [9] to calculate the correlation between patches of LR and Ref images. However, relevant experiments indicate that even though Ref images have authentic high-frequency details, the network cannot completely transform these details into HR images. Theoretically, the cross-attention (CA) method only consider the positional information but ignore the variety of the scale of foreground, which need alignment. There are two specific cases: 1) When the foregrounds between the LR and Ref image have different scale, the patch will contain different areas of the foreground. Even if the foregrounds of the LR and Ref image have same semantic information, this situation leads to mismatch because of the inconsistent scale, as illustrated in Fig. 1(a).

2) Even if the scale in LR and Ref image is the same, the cross-attention method (CA) ignores whether the scale of the patch size fits the foreground. Although the patch size is fixed, the foreground scale is various. Therefore, the patch size is hard to fit the foreground scale. For example, if the foreground size is smaller than patch size, the patch will contain massive amounts of information, further interfering the calculation of the correlation matrix, as illustrated in Fig. 1(b). If the patch size is too small, different patches will mismatch due to the similarity of local features, as illustrated in Fig. 1(c).

Based on this consideration, we propose the Flexible Alignment (FA) module, which includes the Single-Multi Pyramid Alignment module (S-A) and the Multi-Multi Pyramid Alignment module (M-A). The FA module aims at generating various receptive fields to solve the limitation of the image scale. Additionally, we fuse the multi-scale features with the Cross-Hierarchical Progressive Fusion (CHPF) module, further improving the image quality. Furthermore, fourier loss function is introduced to optimize the model. Our contributions can be summarized as follows:

- We propose the FASR-Net to leverage the MRI dataset by transforming the textural information of high-resolution PD

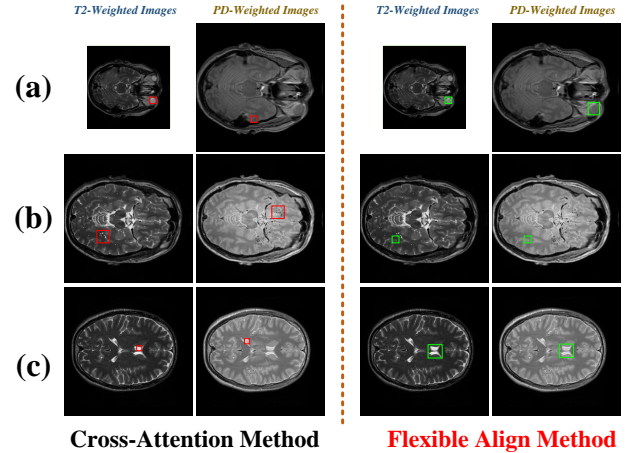


Fig. 1. The comparison between Cross Attention method (CA) and our Flexible Align method (FA). FA contains two parts: S-A module and M-A module. Specifically, when the scale of LR and Ref images is different, S-A module will adjust the mismatch produced by CA, as shown in (a). M-A module solves the mismatch caused by the inappropriate patch size. If the patch size is too large, the similarity between patches will be dominated by background noise, which is illustrated in (b). When the patch size is too small, the insufficient semantics will lead to mismatch, which is denoted in (c).

images into low-resolution T2 images and making the texture more realistic.

- Our model jointly combines the Multi-Multi Pyramid Alignment module (M-A) and the Single-Multi Pyramid Alignment module (S-A) to align LR image and Ref image at different scales.

- We introduce an effective feature fusion backbone Cross-Hierarchical Progressive Fusion (CHPF) which takes advantage of textural information and details of multi-scale features.

- We adopt an additional Fourier loss function to optimize our network, which is effective in the recovery of high-frequency information.

Our code will be available at [FASR-Net](#).

II. RELATED WORK

A. Single Image Super-Resolution

For the past few years, deep learning-based SISR methods have performed amazing performances. Lu *et al.* propose SRCNN [10], which introduces deep convolutional neural networks in the field of image Super-Resolution. Thereafter, residual blocks and attention mechanisms are introduced to deepen the network, such as SAN [11], RCAN [12], and RDN [13]. However, these approaches improve the image quality restrictedly. Additionally, it is challenging to recover high-frequency details. Christian *et al.* [14] firstly adopt Generative Adversarial Network (GAN) in SR tasks. According to Christian, minimizing the mean squared loss (MSE) often lacks high-frequency details. Thus, [14] utilizes the perceptual loss, which consists of content loss and adversarial loss. Wang *et al.* [15] further propose enhanced generator and discriminator obtaining more perceptually competitive results. Knowledge distillation framework is also introduced in SR

tasks, such as [16], [17]. Recently, some Transformer-based networks have been applied to SISR tasks [3], [4]. ESRT [3] adopts a high-preserving block and lightweight transformer backbone, achieving satisfying results with low computational cost. SwinIR [4] adopts shifted-window-based self-attention mechanism in Swin Transformer [18].

Although SISR approaches achieve marvelous results in the natural image domain, these methods lack the ability to generate high-frequency information, which will cause blurry effects. Additionally, the details of HR images, which are significant for diagnosis, are generated by networks but are not authentic. The reasonable method for MRI Super-Resolution is complementing high-frequency information from additional HR images. Therefore, Ref-SR methods are more likely to achieve believing methods for medical images.

B. Reference-Based Image Super-Resolution

Ref-SR adopts an additional high-resolution reference image to resolve low-resolution image. Compared with SISR, Ref-SR is more likely to harvest accurate textural information. One branch of Ref-SR methods is to align LR and Ref images. CrossNet [19] adopts an end-to-end and fully-convolutional neural network with the optical flow estimator to align Ref images and LR images. However, this approach depends on the alignment of Ref images and LR images to a great extent. Additionally, the utilization of optical flow neglects the long-range dependencies. SSEN [20] introduces a stack of deformable convolution [21] layers, enlarging the receptive field of Ref images. C^2 -matching [22] introduces the contrastive correspondence network and teacher-student correlation distillation to align images on pixel level. However, because the restoration module of C^2 -matching contains only simple residual blocks, the misalignment between images will drastically destroy the performance of this method.

Another mainstream of Ref-SR approaches is based on patch matching [6]. SRNTT [8] adopts cross-attention mechanism to achieve patch matching, which endows LR images with HR details by transferring textural information from Ref images according to the correlation. Further, TTSR [9] retains the idea of cross-attention and introduces soft-attention module which computes the relevance between original and swapped features, feeding all swapped features with different weights into the main network. Furthermore, cross-scale feature integration module stacks multiple texture transformers and improves the performance of TTSR further. MASA [23] takes the potential enormous difference, such as color and luminance distribution, into consideration and reduces the computational cost.

III. METHOD

A. Overview

The Reference-based Super-Resolution Reconstruction (Ref-SR) method has become very popular recently, transforming details of high-resolution reference (Ref) images into low-resolution (LR) images. The details recovered by the Ref-SR method are more reliable than the conventional generative models.

To observe a tissue clearly, a series of multi-contrast images will be produced together during the acquisition of MRI. When the image is blurred or low-resolution, in the process of SR reconstruction, a intuitive thought is that the adjacent images can be used as references to offer helpful detail information. Therefore, we propose a novel Multi-Contrast Flexible Alignment Super-Resolution Network (FASR-Net) for MRI. The architecture of FASR-Net is shown in Fig. 2. FASR-Net receives $\mathbf{I}_{LR\uparrow}$, $\mathbf{I}_{Ref\downarrow\uparrow}$ and \mathbf{I}_{Ref} as inputs. In our research, we utilize PD-weighted images (denote as \mathbf{I}_{Ref}) as supplementaries to reconstruct high-resolution T2-weighted images (denote as \mathbf{I}_{SR}) from low-resolution T2-weighted images (denote as \mathbf{I}_{LR}). $\mathbf{I}_{LR\uparrow}$ is the $4\times$ upsampled of the T2-weighted image. We sequentially apply downsampling and upsampling with the same factor $4\times$ on Ref to obtain $\mathbf{I}_{Ref\downarrow\uparrow}$ which is domain-consistent with $\mathbf{I}_{LR\uparrow}$.

The FASR-Net can be roughly divided into three parts:

- 1) Shallow feature extractor extracts robust semantic features from the inputs. Subsequently, the features will be sent into the FA module. To simplify the expression, we similarly denote the features as $\mathbf{I}_{LR\uparrow}$, $\mathbf{I}_{Ref\downarrow\uparrow}$ and \mathbf{I}_{Ref} .
- 2) The Flexible Alignment (FA) module consists of two parts: Single-Multi Pyramid Alignment module (S-A) and Multi-Multi Pyramid Alignment module (M-A).

The two parts of FA modules are expressed as Eq. (1)-(2):

$$\mathbf{F}_{SA} = \mathcal{F}_{S-A}(\mathbf{I}_{LR\uparrow}, \mathbf{I}_{Ref}, \mathbf{I}_{Ref\downarrow\uparrow}) \quad (1)$$

$$\mathbf{F}_{MA} = \mathcal{F}_{M-A}(\mathbf{I}_{LR\uparrow}, \mathbf{I}_{Ref}, \mathbf{I}_{Ref\downarrow\uparrow}) \quad (2)$$

Where \mathcal{F}_{S-A} represents the Single-Multi Pyramid Alignment module (S-A) and \mathcal{F}_{M-A} indicates the Multi-Multi Pyramid Alignment module (M-A).

- 3) The Cross-Hierarchical Progressive Fusion (CHPF) module is shown in Eq. (3), where \mathbf{I}_{SR} represents the reconstructed high-resolution image.

$$\mathbf{I}_{SR} = \mathcal{F}_{CHPF}(\text{Concat}(\mathbf{F}_{MA}, \mathbf{F}_{SA})) \quad (3)$$

B. Texture Extractor

The FASR-Net doesn't adopt current transformer-based methods [24], [25], [26], [18], [27], [28], which directly unfold the raw image to patches and feed into word-embedding. Due to the unconstrained property of self-attention, training process is complex and massive data is necessary for converging the transformer. The paranoid inductive convolution property can compensate for the defect that the transformer only supports the global response [29]. Therefore, the CNN-based backbone was first used to perform a texture extractor.

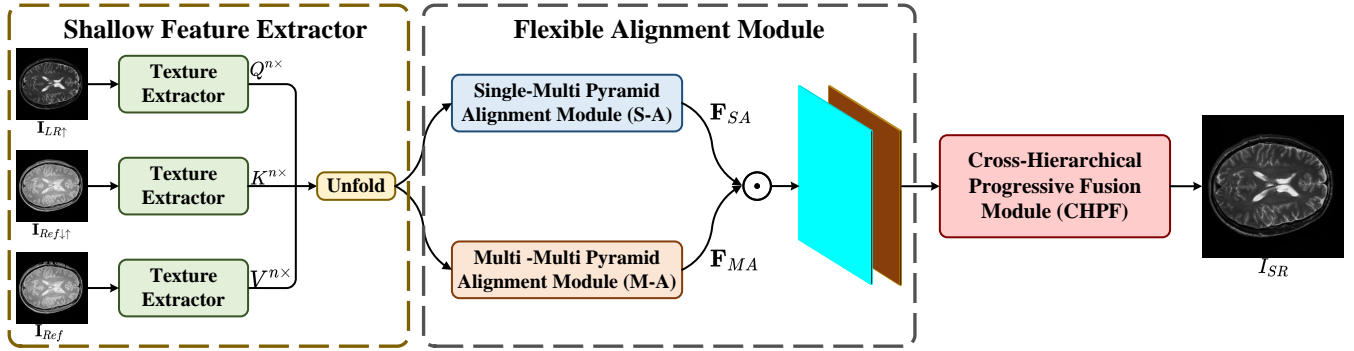


Fig. 2. The overview of RCFA-Net. RCFA-Net is composed of three parts: the shallow feature extractor, the Flexible Alignment module, and the Cross-Hierarchical Progressive Fusion module. $Q^{n \times}$, $K^{n \times}$, and $V^{n \times}$ are multi-scale shallow features extracted from $I_{LR\uparrow}$, $I_{Ref\downarrow\uparrow}$, and I_{Ref} . The S-A and M-A are two parts of the Flexible Alignment module introduced in Section III C. F_{SA} and F_{MA} are respectively aligned features produced by S-A and M-A module. After concatenating the features, the Cross-Hierarchical Progressive Fusion module is utilized to reconstruct the I_{SR} .

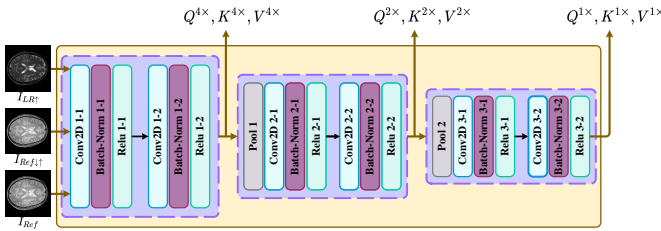


Fig. 3. We adopt a pretrained VGG-19 network as the texture extractor. $4 \times$ feature, $2 \times$ feature and $1 \times$ feature are respectively extracted from ReLU 1-2, ReLU 2-2 and ReLU 3-2. Note that the parameters of texture extractor will be finetuned in the process of training.

In the following alignment process, not each pixel of the Ref image can exactly correspond to the local part of the LR image, so the use of shallow features can compensate for this pixel-by-pixel accuracy and make them semantically align with each other.

Shallow features are extracted by a pre-trained backbone like VGG [30]. In addition, the shallow feature extraction part is relatively independent, which means a structure with a high degree of freedom. We can replace the part of the backbone at will. In this paper, we analyze several well-known backbones by ablation experiments. The process of extracting features can be expressed as Eq. (4)-(6):

$$Q = \mathcal{F}_{TE}(I_{LR\uparrow}) = \{Q^{1 \times}, Q^{2 \times}, Q^{4 \times}\} \quad (4)$$

$$K = \mathcal{F}_{TE}(I_{Ref\downarrow\uparrow}) = \{K^{1 \times}, K^{2 \times}, K^{4 \times}\} \quad (5)$$

$$V = \mathcal{F}_{TE}(I_{Ref}) = \{V^{1 \times}, V^{2 \times}, V^{4 \times}\} \quad (6)$$

Where \mathcal{F}_{TE} denotes the texture extractor. The extracted texture features, Q (*query*), K (*key*) and V (*value*), indicate three basic elements of the Flexible Alignment Module.

C. Flexible Alignment (FA) Module for Feature Maps

The Flexible Alignment (FA) module takes the extracted features produced by the shallow feature extractor as inputs and outputs a synthesized feature map, which will be further used to generate the HR prediction.

Image alignment, which is also known as image registration in medical imaging, maps some high-frequency details of the Ref image to the most relevant LR image parts. This mapping can be viewed as a series of affine transformation operations, which mainly include: clipping, position translation, and scaling.

- In the aspect of clipping, a patch with a fixed size is taken as the clipping unit.
- In the aspect of position-translation, we mainly select the patches with the highest similarity between the two images. This operation inherits the core from cross-attention mechanism.
- In terms of scale, since the size of patch is fixed, it inevitably limits the flexibility of the receptive field. We have two considerations to adjust the receptive field of the feature map, which are the key points to be addressed in this chapter and the most innovative part of this paper.

1) *The Single-Multi Pyramid Alignment module (S-A) for different image scale*: When the $I_{LR\uparrow}$ and $I_{Ref\downarrow\uparrow}$ have different image scales, the FA module will calculate the similarities between the patches. One patch contains global foreground information, but the other patch may only contain local foreground information. It will lead to a mismatch even though the foregrounds of the LR image and Ref image are very similar, as seen in Fig. 1(a). To solve this problem, we propose the Single-Multi Pyramid Alignment module (S-A) to endow $I_{Ref\downarrow\uparrow}$ with flexible receptive fields. The operation takes full advantage of the patches with different scales, as illustrated in Fig. 4.

The S-A module generates $q^{4 \times}$, $k^{n \times}$, and $v^{n \times}$ during word embedding, the process can be expressed as:

$$q^{4 \times} = \mathcal{F}_{WE-q}(Q^{4 \times}) \quad (7)$$

$$k^{n \times} = \mathcal{F}_{WE-k}(K^{n \times}) \quad (8)$$

$$v^{n \times} = \mathcal{F}_{WE-v}(V^{n \times}) \quad (9)$$

Where $n = \{1, 2, 4\}$, which represents the factor $1 \times$, $2 \times$ and $4 \times$ of texture feature extracted from different depth of the backbone, as can be seen in Fig. 3.

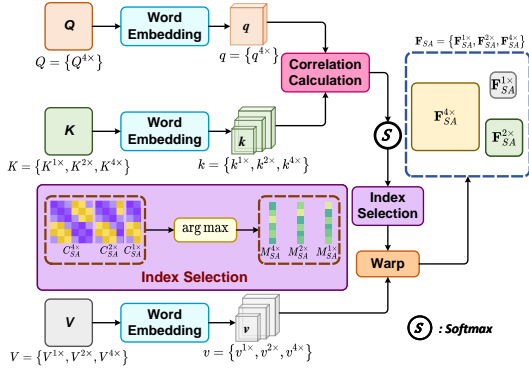


Fig. 4. The architecture of S-A in detail. The process of index selection is shown in the purple rectangle. The input $Q^{4 \times}$, $K^{n \times}$, and $V^{n \times}$ are fed into word embedding to match the shape. Note that word embedding contains both unfold and linear layer. Through the correlation calculation between $q^{4 \times}$ and $k^{n \times}$, we can obtain $C_{SA}^{n \times}$. Then $k^{n \times}$ will warp with the indication of corresponding $M_{SA}^{n \times}$, which is implemented by the index selection of $C_{SA}^{n \times}$.

The alignment process is in the purple rectangle of Fig. 4, where we calculate the patch position by similarity degree. Inspired by the cross-attention mechanism [31], we generate $C_{SA}^{n \times}$ matrix, which represents the correlation between different embedded patches from $q^{4 \times}$ and $k^{n \times}$, which can be seen in Eq. (10).

$$C_{SA}^{n \times} = \mathbf{Softmax}(\langle q^{4 \times}, k^{n \times} \rangle, dim = 1) \quad (10)$$

Traditional attention mechanism takes a weighted sum of value for each query. However, such an operation may cause blur effect which lacks the ability of transferring texture features. Therefore we create $M_{SA}^{n \times}(i)$, which only save the index of position with max weight of each row in $C_{SA}^{n \times}$ matrix, as illustrated in Eq. (11). Then we use $M_{SA}^{n \times}(i)$ matrix to warp the $V^{n \times}$, as seen in Eq. (12). The warp operation means the embedded patches with important detail information on the Ref image are preserved and those with few reference value are obliterated. The output of S-A module $F_{SA}^{n \times}$ is summarized in Eq. (13).

$$M_{SA}^{n \times}(i) = \arg \max_j C_{SA}^{n \times}(i, j) \quad (11)$$

$$F_{SA}^{n \times} = v^{n \times}(M_{SA}^{n \times}(i)) \quad (12)$$

$$F_{SA} = \{F_{SA}^{1 \times}, F_{SA}^{2 \times}, F_{SA}^{4 \times}\} \quad (13)$$

Where (i, j) denotes the index of 2D tensors ($C_{SA}^{n \times}(i, j)$), (i) represents the row index of 2D tensors ($v^{n \times}$) and the index of 1D tensors ($M_{SA}^{n \times}$).

2) *The Multi-Multi Pyramid Alignment (M-A) module for the same image scale*: We introduce the Multi-Multi Pyramid Alignment (M-A) module when the texture features of $I_{LR \uparrow}$ and $I_{Ref \downarrow}$ have the same image scale. The patch size is fixed at the clipping level, which limits the scalability of the texture feature of foreground. When the proportion of foreground in the patch is small, even if $I_{LR \uparrow}$ and $I_{Ref \downarrow}$ have high similarity in the foreground, it will still fail to match due to the interference of different backgrounds, as seen in Fig. 1(b) and Fig. 1(c). To ensure the scalability of the proportion of

foreground in the patch, we introduce M-A module, as shown in Fig. 5.

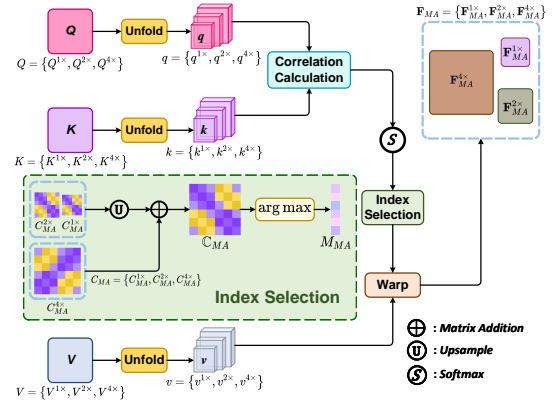


Fig. 5. The architecture of S-A in detail. The process of index selection is shown in the green rectangle. The inputs $Q^{n \times}$, $K^{n \times}$ and $V^{n \times}$ are unfolded to multi-scale two-dimensional tensors (Note that the batch dimension is discarded from notations for simplicity). Because the shape of matrix ($C_{MA}^{n \times}$) row is different, we upsample the matrixes to match the shape. Subsequently, all multi-scale $v^{n \times}$ warp with the order of M_{MA} .

$M - A$ receives query $Q^{n \times} \in \mathbb{C}^{f_n \times w \times h}$, key $K^{n \times} \in \mathbb{C}^{f_n \times w \times h}$ and $V^{n \times} \in \mathbb{C}^{f_n \times w \times h}$ as the inputs. Subsequently, we unfold the inputs into two-dimensional tensors $q^{n \times} \in \mathbb{C}^{f_n \times wh}$, $k^{n \times} \in \mathbb{C}^{f_n \times wh}$ and $v^{n \times} \in \mathbb{C}^{f_n \times wh}$. The M-A structure endows the fixed-size patch with flexible receptive fields to fit the foreground size.

Eq. (14) performs the similarity response in the M-A module. The response $C_{MA}^{n \times}$ matrixes can form a new pyramid structure. To match the different shapes of $C_{MA}^{n \times}$, we use $C_{MA}^{n \times}$ to C_{MA} by upsampling the pyramid structure as the same scale, where \mathcal{U} represents upsampling.

$$C_{MA}^{n \times} = \mathbf{Softmax}(\langle q^{n \times}, k^{n \times} \rangle, dim = 1) \quad (14)$$

$$C_{MA} = \mathcal{U}(C_{MA}^{1 \times}) + \mathcal{U}(C_{MA}^{2 \times}) + C_{MA}^{4 \times} \quad (15)$$

Similar to S-A, we sort the rows of C_{MA} matrix and generate $M_{MA}(i)$ by preserving the position with max weights. Thus, we acquire F_{MA} , as shown in the Eq. (16).

$$F_{MA} = \{F_{MA}^{1 \times}, F_{MA}^{2 \times}, F_{MA}^{4 \times}\} \quad (16)$$

D. The Cross-Hierarchical Progressive Fusion module (CHPF)

After the Flexible Alignment (FA) module, the texture feature has been completely aligned in various scales thanks to the pyramid model structure. In the final feature fusion stage, we propose a Cross-Hierarchical Progressive Fusion module (CHPF) to fuse the features of different scales and restore I_{SR} . As shown in Fig. 6, the input of the CHPF module is $F_{MS}^{n \times}$, which is generated by Eq. (17). $F_{MA}^{n \times}$ and $F_{SA}^{n \times}$ represent the outputs of FA module. In order to consider multi-scale features (include $1 \times$, $2 \times$ and $4 \times$ features), $F_{MS}^{n \times}$ of various scale will map to the same size by up/down sampling

in fully-connection convolutional layer. In addition, the fully-connection convolutional layer will also fuse the $\mathbf{F}_{MS}^{n \times}$ by 1×1 convolution, denoted by straightforward.

$$\mathbf{F}_{in}^{n \times} = \text{Concat}(\mathbf{F}_{MA}^{n \times}, \mathbf{F}_{SA}^{n \times}) = \{\mathbf{F}_{in}^{1 \times}, \mathbf{F}_{in}^{2 \times}, \mathbf{F}_{in}^{4 \times}\} \quad (17)$$

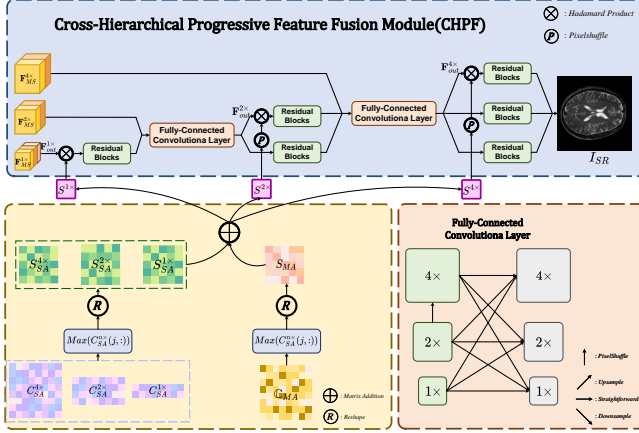


Fig. 6. The backbone of CHPF is shown in the top rectangle. To take full advantage of multi-scale features, $1 \times$, $2 \times$ and $4 \times$ features will fuse in CHPF. To match the shapes, we adopt the fully-connected convolutional layer to merge multi-scale features, as illustrated at the bottom-right corner. Note that we also introduce soft-attention mechanism, which means $S^{n \times}$ indicates the level of transferred texture information. The calculation of $S^{n \times}$ is shown in the yellow rectangle.

In fact, each scale of $\mathbf{F}_{out}^{n \times}$ has transferred texture information with different levels. During feature fusion, we should treat them discriminatively. Therefore, each scale of $\mathbf{F}^{n \times}$ will be modulated by soft-attention mechanism, as can be seen in Eq. (21). Soft-weight matrixes ($S^{n \times}$) are generated from both the S-A and the M-A modules, as shown in Eq. (18)-(20).

$$S_{SA}^{n \times}(i) = \max_j C_{SA}(i, j) \quad (18)$$

$$S_{MA}^{n \times}(i) = \max_j C_{MA}(i, j) \quad (19)$$

$$S^{n \times} = S_{SA}^{n \times} + S_{MA}^{n \times} \quad (20)$$

$$\mathbf{F}^{n \times} = \mathbf{F}_{out}^{n \times} \otimes S^{n \times} \quad (21)$$

Where \otimes represents matrix multiplication.

E. Loss

1) **L1 Loss:** To distinguish the differences between the high-resolution reconstructed image (\mathbf{I}_{SR}) and ground truth (\mathbf{I}_{HR}), a practical method is calculating the pixel-level difference between the two images. This method can guide FASR-Net to pay more attention on the details of the image, such as texture, color, and blurred information. Many previous experiments have proved its effectiveness [32], [33]. We choose L1 loss to act as a pixel-level loss in FASR-Net. It acts as an essential part of the total loss. For details of the L1 loss, see Eq. (22). The total loss can be seen in Eq. (25). Where \mathbf{I}_{HR} represents ground truth, and \mathbf{I}_{SR} represents the image that was repaired.

$$\mathcal{L}_1 = |\mathbf{I}_{SR} - \mathbf{I}_{HR}| \quad (22)$$

2) **Perception Loss:** However, using the L1 loss alone is limited. It will focus only on local detail but ignore the global information. Besides that, it can also lead to artifacts. For instance, considering two identical images offset by one pixel from each other, although they are similar in perception, the results will be very different. Based on this consideration, the FASR-Net will calculate the differences in the high-level semantic feature map. So we incorporate the Perceptual loss [34] into the total-loss function to loosen the restrictions of using L1 loss alone. This Perceptual loss calculates the least-square distance between ground truth and the repaired image based on the feature map, which is extracted by the VGG-19 network [30]. The receptive field of each pixel in the feature map corresponds to the 8×8 adjacent fields of the original map. The process is shown in Eq. (23).

$$\mathcal{L}_P = [\text{vgg}(\mathbf{I}_{SR}) - \text{vgg}(\mathbf{I}_{HR})]^2 \quad (23)$$

3) **Fourier Transform Loss:** Since the purpose of image Super-Resolution is more critical to the reconstruction of the lost high-frequency components, it is crucial to reduce the variance in the frequency domain. Consequently, we apply a Frequency Reconstruction (FR) loss, as can be seen in Eq. (24).

$$\mathcal{L}_{FR} = \|F(\mathbf{I}_{SR}) - F(\mathbf{I}_{HR})\|_1 \quad (24)$$

F denotes the fast Fourier transform (FFT) that transfers the image signal to the frequency domain. The final loss function for training our network is determined as follows:

$$\mathcal{L}_{total} = \mathcal{L}_1 + \mathcal{L}_P + \mathcal{L}_{FR} \quad (25)$$

IV. EXPERIMENTS

A. Datasets

1) **IXI:** The IXI dataset [35] is a collection of MR images from 578 patients, including T1, T2, and PD-weighted images and others. The T1, T2, and PD images obtained from the same region each contain special textural details. If every single image can be utilized properly, a higher resolution image can be generated.

Our experiment uses downsampled T2 images as inputs, original T2 images as ground truth (GT), and corresponding PD images as reference. Specifically, the original size of both T2 and PD images in the IXI dataset are $256 \times 256 \times 3$. The LR images are created by downsampling. For example, to achieve the $4 \times$ scale of SR results, its size should be $64 \times 64 \times 3$. Before training, all images are normalized over the range of $[-1, 1]$. We filter out 14000 and 1000 pairs of T2 and PD-weighted images for training and validation, respectively.

2) **FastMRI:** The FastMRI dataset [36] contains four types of data from MRI acquisitions of knees and brains, aiming to connect the data science and the MRI research communities. The Knee MRI subset embodies raw data from more than 1,500 fully sampled knee MRIs obtained on 3 and 1.5 Tesla magnets, and DICOM images from 10,000 clinical knees MRIs also obtained at 3 or 1.5 Tesla. The Brain MRI collects 6,970 fully sampled brain MRIs obtained on 3 and 1.5 Tesla magnets. It must be mentioned that the shape of original images varies for different patients. We filter out 600 and 58

pairs of PD and FS-PDWI (Fat Suppression Proton Density-Weighted images which have been aligned to 256x256x3 for training and validation. The other configuration is in accord with the IXI training protocol.

B. Implementation Details

We start with a batch size of 4 and the Adam optimizer with a learning rate of $1e-4$ for the feature extractor backbone. As for the rest network parameters, the learning rate is set to $1e-5$. We use a pre-trained Vgg19 feature extractor component as the backbone of FASR-Net. In the training process, the solely L1 loss function is applied during the initial 10 epochs to obtain a coarse model, and in the subsequent 50 or more epochs, all the proposed losses are employed to fine-tune the model. All the work was implemented using PyTorch1.10 on an RTX 3090 GPU.

C. Comparison with the SOTA

To demonstrate that our proposed model can achieve better SR results, we compare the experimental results on IXI and FastMRI, respectively. We employ PSNR and SSIM as criteria to evaluate the effectiveness of our method.

1) *IXI Dataset*: We compare our results with several previous works on the IXI dataset, including ELCP [37], T2Net [38], MCSR [39], SwinIR [4], MINet [5], TTSR [9] and MASA [23]. Fig. 7 reports the metrics scores with IXI dataset under $2\times$ and $4\times$ enlargement. As can be seen, our approach achieves the best performance compared with the existing method. ELCP [37] use a convolutional neural network to integrate diverse SR results from individual models, combining multiple GAN models trained on the different image prior datasets. However, it can be found that the effect is not ideal in extensive multiple Super-Resolution repairs. T2Net [38] combines reconstruction and Super-Resolution and encourages joint feature learning between the two tasks. However, no reference information was used compared with us, so the repair effect was not optimistic. SwinIR [4] adopts swin-transformer as feature extractor and utilize a common decoder to obtain SR results. Due to the robust feature extracted by swin-transformer, this method achieves best results among the SISR methods. Notably, the SISR methods are far less effective than the Ref-SR models. MCSR [39] exploits a contrasting HR image of a different modality as a reference. A CNN-based MCSR-processing step is proposed to improve the quality of the reconstructed further. However, there is still some gap compared with our model due to the lack of accurate feature fusion for reference details. MINet [5] learns a hierarchical feature representation from multiple convolutional stages for each different-contrast image, and good results are obtained with the help of reference images. TTSR [9] and MASA [23] introduces align module. Therefore, these methods obtain more effective results.

In Fig. 8, we use the $4\times$ scale output I_{SR} and the corresponding residual maps to show our model’s best visual effect. The residual maps, also named error maps, represent the absolute pixel-value differences between the output results from each method and the ground truth of the T2-weighted HR

image. The smaller the difference, the closer the two images are, which means the better reconstruction performance the model achieves.

2) *FastMRI Dataset*: We compare our results with several previous works on the FastMRI dataset, including EDSR [40], MCSR [39], MINet [5], TTSR [9], MASA [23] and SwinIR [4].

TABLE I
QUANTITIVE COMPARISON ON THE FASTMRI DATASET

Scale	$2\times$		$4\times$	
Metrics	PSNR	SSIM	PSNR	SSIM
Bicubic	23.141	0.714	19.202	0.645
EDSR (2017,CVPR) [40]	30.124	0.851	26.719	0.725
MCSR (2020, TMI) [39]	35.021	0.897	29.542	0.816
TTSR (2020, CVPR) [9]	35.712	0.909	32.018	0.880
MINet (2021, MICCAI) [5]	35.917	0.926	31.974	0.876
MASA (2021, CVPR) [23]	36.817	0.934	32.965	0.842
SwinIR (2021, ICCV) [4]	37.729	0.957	32.971	0.849
FASR (Ours)	38.231	0.964	33.403	0.861

The corresponding visual effects are displayed in Fig. 9, the differential effect between our result and ground truth can be easily found in the residual map. The lighter the color is in the residual map, the better the effect is.

D. Ablation Study

To find the optimal network structure, we established a study of 3 sets of ablation experiments. In the first study, the effect of the backbone on the model is mainly compared. The second ablation experiment verifies the effectiveness of the proposed modules of this algorithm. The third ablation experiment evaluates the effect of different loss functions on the image inpainting effect.

TABLE II
ABLATION STUDY OF SHALLOW FEATURE EXTRACTOR BACKBONE

Backbone	# Params(M)	# FLOPs(G)	PSNR	SSIM
resnet18	12.87	32.04	38.55	0.959
resnet34	22.51	68.09	38.70	0.965
vgg19	12.34	22.06	38.52	0.974

1) *Shallow Feature Extractor Backbone Ablation*: To determine the influence of different backbone architectures on PSNR and SSIM scores, we selected three widely used feature extractor networks and conducted three experiments on the IXI dataset. We summarized the number of parameters, FLOPs, PSNR, and SSIM scores in Tab. II. The resnet34 feature extraction module achieves the best results because of its huge FLOPs and parameters. Resnet18 has a slight performance improvement compared to VGG19. However, at the same time, this method requires more computation. To make the number of feature channels of each output layer of each model the same, we modified the feature map channels of the network based on the resnet source code. So the number of parameters

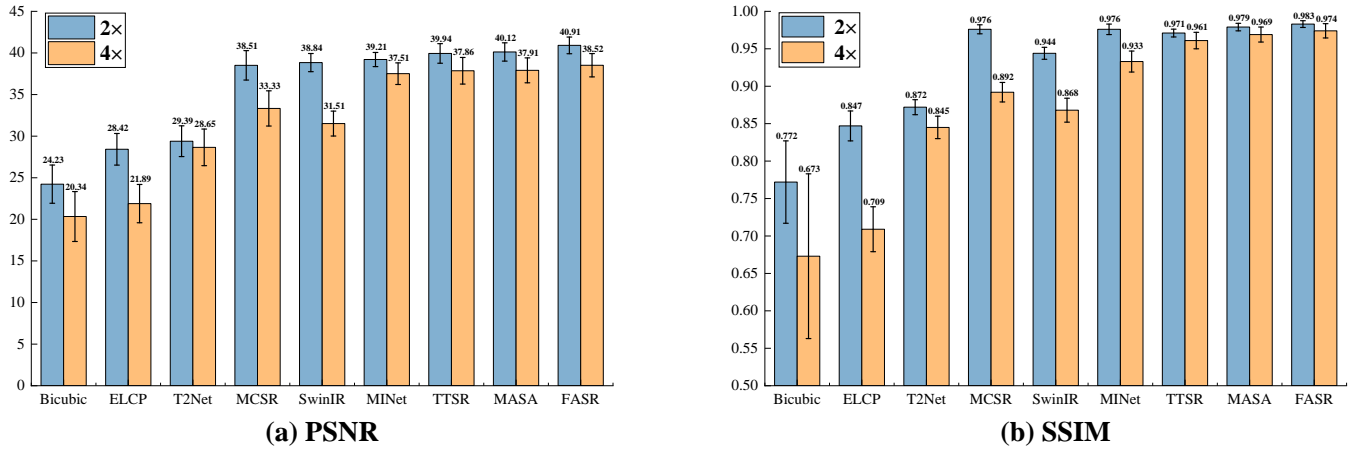


Fig. 7. The quantitative metrics of IXI dataset under 2 \times and 4 \times enlargement.

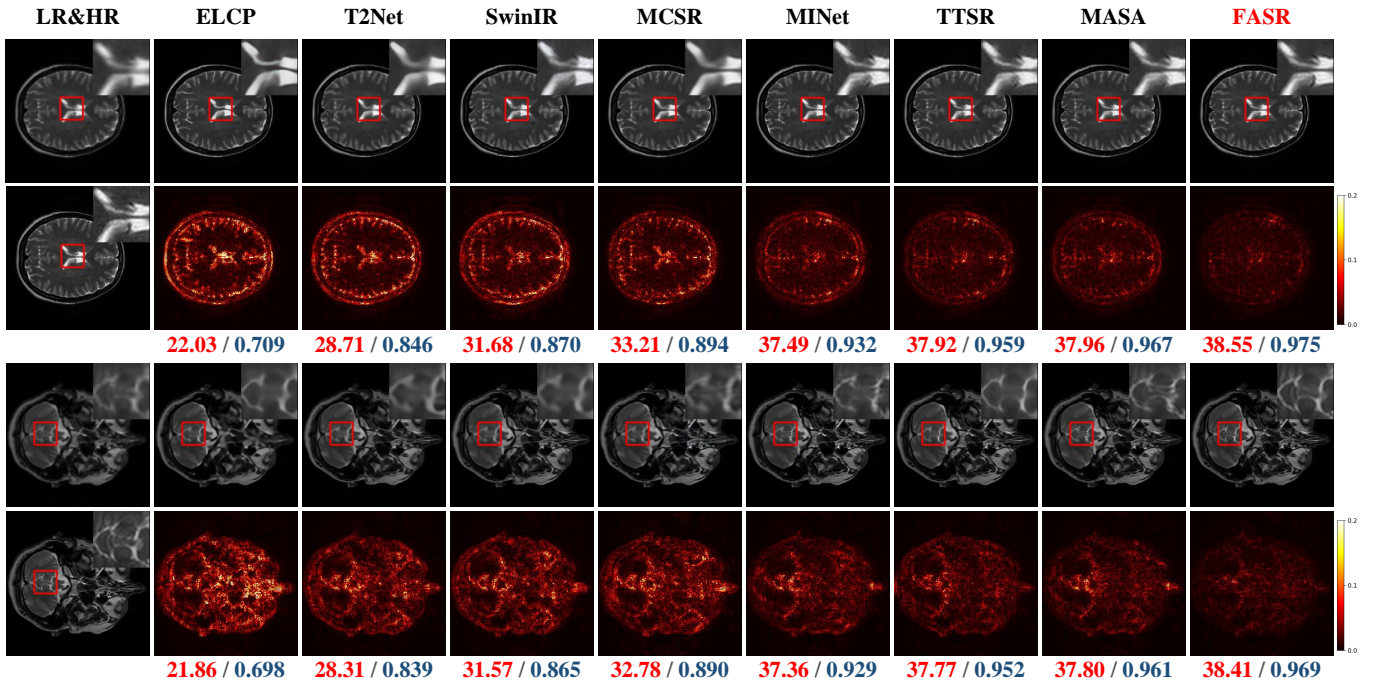


Fig. 8. Visual comparison of the output and residual maps from different model on the IXI dataset under 4 \times enlargement. The residual map measures the absolute value of pixel-value disparities between the output of the model and corresponding ground truth. LR represents low-resolution images which generated by downsampling. HR represents the ground truth.

and FLOPs will be inconsistent with those officially provided by Resnet. In addition, the parameters in the feature extractor layer of each model are counted, and the FLOPs are quantified by processing a $256 \times 256 \times 3$ shaped image.

2) Effectiveness of Proposed Modules : In the second set of ablation experiments, we control a single variable to evaluate the effectiveness of the proposed module, including 1) The Multi-Multi Pyramid Alignment module (M-A); 2) The Single-Multi Pyramid Alignment module (S-A); 3) The Cross-Hierarchical Progressive Fusion module (CHPF); 4)

Flexible Alignment module (FA) combines the S-A and M-A modules. The quantitative results are shown in Tab. III, and the qualitative visual effects are shown in Fig. 10 .

In the W/O S-A experiment, we removed the S-A module so that the Flexible Alignment module (FA) retained only the M-A module. Compared with the experimental results of the complete structure, both PSNR and SSIM indexes are reduced. It is mainly because when the feature map of the reference image (Ref) and low-resolution image (LR) have different scales in the receptive field, the module of S-A can

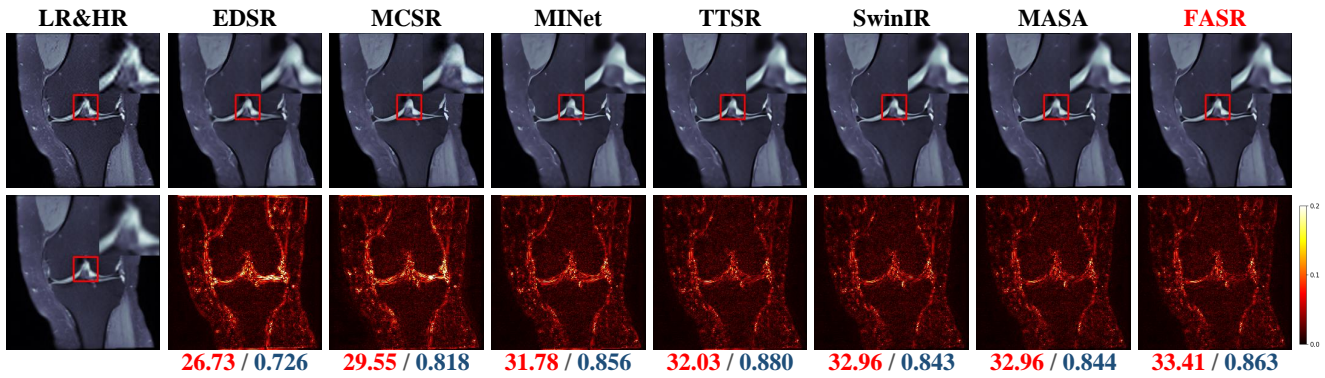


Fig. 9. Visual comparison of the output and residual maps from different models on the FastMRI dataset under $4\times$ enlargement.

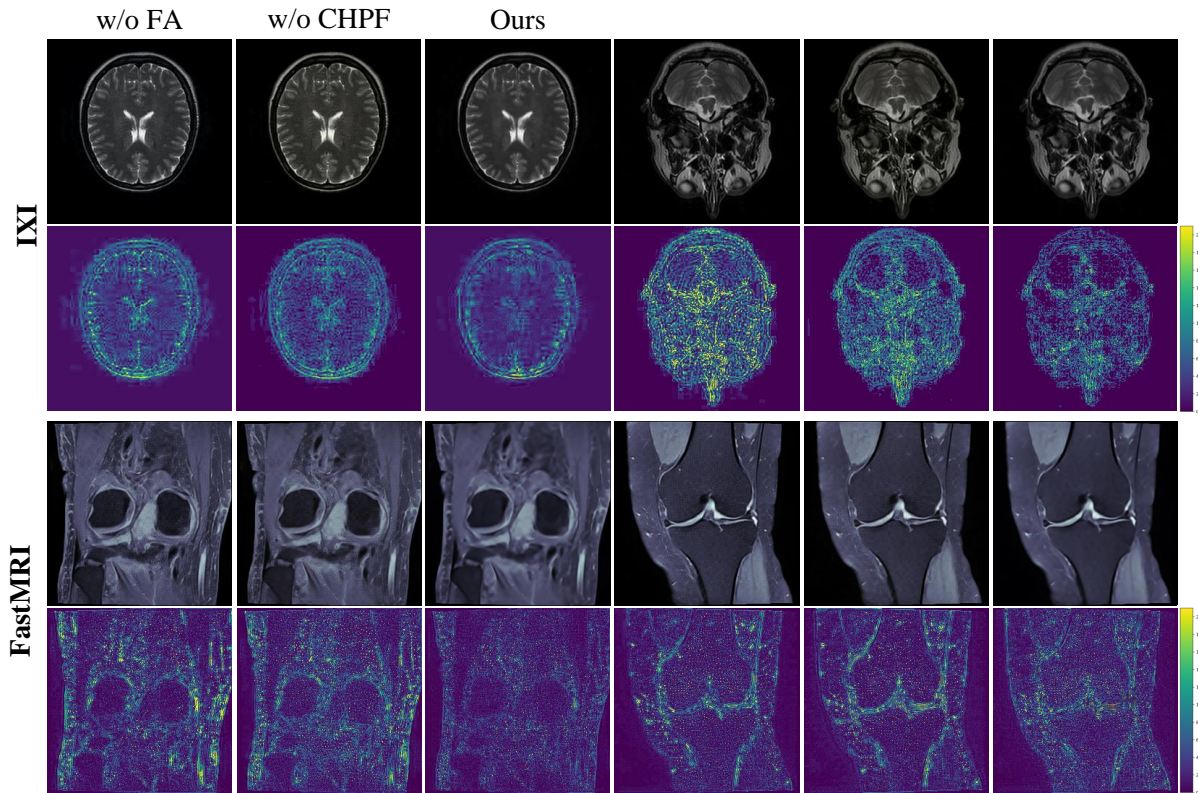


Fig. 10. Visual comparison of the output and residual maps from different models under $4\times$ enlargement on the IXI and FastMRI dataset, respectively.

adaptively balance it to ensure complete feature alignment. In contrast, W/O M-A removes the M-A module and only retains the S-A module in the FA module. The S-A module ensures that the patch's foreground is consistent with the patch's size to avoid excessive background blending. However, this group of experimental indicators declined more seriously, indicating that M-A had a better effect on the feature alignment than S-A. In the W/O FA experiment, the Flexible Alignment module, which includes both M-A and S-A alignment modules, was replaced by cross-attention. Owing to the limitation of the receptive field, cross-attention exhibits the worst performance in the alignment model, which also indicates the common

effectiveness of S-A and M-A. The W/O CHPF model uses a decoder to directly restore the aligned features and ignores the fusion of multi-hierarchical feature maps, which also has a poor experimental effect on the IXI testset.

In addition, Fig. 11 shows the stability in performance of w/o FA, w/o CHPF, and the complete model during the training process. The three models have similar improvement performance at the time point indicated by the red dotted line, but the complete model has more room for improvement after the subsequent learning rate is gradually reduced.

3) *Loss Ablation*: The third set of ablation experiments is to verify the impact of different loss functions on the quality

TABLE III

QUANTITIVE COMPARISON OF PROPOSED MODULES ON THE IXI DATASET

	S-A	M-A	CHPF	PSNR	SSIM
w/o S-A		✓	✓	38.12	0.961
w/o M-A	✓		✓	37.93	0.953
w/o CHPF	✓	✓		35.14	0.907
w/o FA			✓	35.06	0.898
complete	✓	✓	✓	38.52	0.974

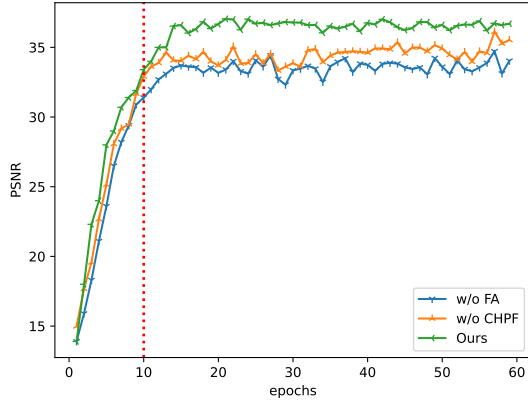


Fig. 11. The PSNR curve for the ablation models: Effectiveness of Flexible Alignment module and Cross-Hierarchical Progressive Fusion module during training. The results are obtained on the IXI dataset with 4x enlargement.

of restored images. As seen in Tab. IV, in the absence of L1 loss, the effect of the model falls off dramatically. This is mainly because in the Super-Resolution process, the pixel-by-pixel loss can largely ensure the stability of the image structure to be repaired and the authenticity of the details, which also demonstrates the importance of L1-loss. In addition, when lacking perceptual loss, the performance of image restoration is also reduced. It is because perceptual loss supervises the reconstructed image at the semantic level so that the network can pay more attention to the accuracy of image semantic information and macroscopically control the trend of image restoration.

Furthermore, in the absence of Fourier loss, it is found that the SSIM score decreases more than PSNR. It is primarily attributed to the that it is easy to operate the high-frequency and low-frequency information of the image separately in the frequency domain, which significantly improves the image's contrast, so it has a more significant impact on the SSIM score. Note that the outcomes are acquired using Vgg19 as the feature extractor backbone.

V. CONCLUSION

In this paper, we have proposed the Flexible Alignment Super-Resolution network for Multi-Contrast MRI images (FASR-Net), which utilizes a related reference image to obtain a more authentic output.

TABLE IV

ABLATION STUDY OF LOSS FUNCTION

\mathcal{L}_1	\mathcal{L}_{per}	\mathcal{L}_{prior}	PSNR	SSIM
	✓	✓	30.93	0.861
✓		✓	36.43	0.952
✓	✓		38.11	0.925
✓	✓	✓	38.52	0.974

Specifically, the Flexible Alignment Module (FA) was proposed to align the semantic features extracted from Ref and LR images by a pre-trained Vgg19 network. FA module can be subdivided into the Multi-Multi Pyramid Alignment module (M-A) and the Single-Multi Pyramid Alignment module (S-A). The M-A module is responsible for aligning input images with the same scale, and S-A deals with the images with different scale. In addition, the Cross-Hierarchical Progressive Fusion (CHPF) module was proposed to progressively fuse the aligned features generated by FA module. At last, extensive experiments on the IXI and the FastMRI datasets proved our method could retain more textural details by comparing with the counterparts obtained by the existing methods in the visual comparison figures.

REFERENCES

- [1] E. Plenge, D. H. Poot, M. Bernsen, G. Kotek, G. Houston, P. Wielopolski, L. van der Weerd, W. J. Niessen, and E. Meijering, "Super-resolution methods in mri: can they improve the trade-off between resolution, signal-to-noise ratio, and acquisition time?" *Magnetic resonance in medicine*, vol. 68, no. 6, pp. 1983–1993, 2012.
- [2] E. Van Reeth, I. W. Tham, C. H. Tan, and C. L. Poh, "Super-resolution in magnetic resonance imaging: a review," *Concepts in Magnetic Resonance Part A*, vol. 40, no. 6, pp. 306–325, 2012.
- [3] Z. Lu, J. Li, H. Liu, C. Huang, L. Zhang, and T. Zeng, "Transformer for single image super-resolution," in *Proceedings of the IEEE/CVF Conference on Computer Vision and Pattern Recognition*, 2022, pp. 457–466.
- [4] J. Liang, J. Cao, G. Sun, K. Zhang, L. Van Gool, and R. Timofte, "Swinir: Image restoration using swin transformer," in *Proceedings of the IEEE/CVF International Conference on Computer Vision*, 2021, pp. 1833–1844.
- [5] C.-M. Feng, H. Fu, S. Yuan, and Y. Xu, "Multi-contrast mri super-resolution via a multi-stage integration network," in *International Conference on Medical Image Computing and Computer-Assisted Intervention*. Springer, 2021, pp. 140–149.
- [6] C. Barnes, E. Shechtman, A. Finkelstein, and D. B. Goldman, "Patch-match: A randomized correspondence algorithm for structural image editing," *ACM Trans. Graph.*, vol. 28, no. 3, p. 24, 2009.
- [7] X. Wang, K. C. Chan, K. Yu, C. Dong, and C. Change Loy, "Edvr: Video restoration with enhanced deformable convolutional networks," in *Proceedings of the IEEE/CVF Conference on Computer Vision and Pattern Recognition Workshops*, 2019, pp. 0–0.
- [8] Z. Zhang, Z. Wang, Z. Lin, and H. Qi, "Image super-resolution by neural texture transfer," in *Proceedings of the IEEE/CVF Conference on Computer Vision and Pattern Recognition*, 2019, pp. 7982–7991.
- [9] F. Yang, H. Yang, J. Fu, H. Lu, and B. Guo, "Learning texture transformer network for image super-resolution," in *Proceedings of the IEEE/CVF conference on computer vision and pattern recognition*, 2020, pp. 5791–5800.
- [10] C. Dong, C. C. Loy, K. He, and X. Tang, "Image super-resolution using deep convolutional networks," *IEEE transactions on pattern analysis and machine intelligence*, vol. 38, no. 2, pp. 295–307, 2015.
- [11] T. Dai, J. Cai, Y. Zhang, S.-T. Xia, and L. Zhang, "Second-order attention network for single image super-resolution," in *Proceedings of the IEEE/CVF conference on computer vision and pattern recognition*, 2019, pp. 11 065–11 074.

- [12] Y. Zhang, K. Li, K. Li, L. Wang, B. Zhong, and Y. Fu, "Image super-resolution using very deep residual channel attention networks," in *Proceedings of the European conference on computer vision (ECCV)*, 2018, pp. 286–301.
- [13] Y. Zhang, Y. Tian, Y. Kong, B. Zhong, and Y. Fu, "Residual dense network for image super-resolution," in *Proceedings of the IEEE conference on computer vision and pattern recognition*, 2018, pp. 2472–2481.
- [14] C. Ledig, L. Theis, F. Huszár, J. Caballero, A. Cunningham, A. Acosta, A. Aitken, A. Tejani, J. Totz, Z. Wang *et al.*, "Photo-realistic single image super-resolution using a generative adversarial network," in *Proceedings of the IEEE conference on computer vision and pattern recognition*, 2017, pp. 4681–4690.
- [15] X. Wang, K. Yu, S. Wu, J. Gu, Y. Liu, C. Dong, Y. Qiao, and C. Change Loy, "EsrGAN: Enhanced super-resolution generative adversarial networks," in *Proceedings of the European conference on computer vision (ECCV) workshops*, 2018, pp. 0–0.
- [16] Q. Gao, Y. Zhao, G. Li, and T. Tong, "Image super-resolution using knowledge distillation," in *Asian Conference on Computer Vision*. Springer, 2018, pp. 527–541.
- [17] W. Lee, J. Lee, D. Kim, and B. Ham, "Learning with privileged information for efficient image super-resolution," in *European Conference on Computer Vision*. Springer, 2020, pp. 465–482.
- [18] Z. Liu, Y. Lin, Y. Cao, H. Hu, Y. Wei, Z. Zhang, S. Lin, and B. Guo, "Swin transformer: Hierarchical vision transformer using shifted windows," in *Proceedings of the IEEE/CVF International Conference on Computer Vision*, 2021, pp. 10012–10022.
- [19] H. Zheng, M. Ji, H. Wang, Y. Liu, and L. Fang, "Crossnet: An end-to-end reference-based super resolution network using cross-scale warping," in *Proceedings of the European conference on computer vision (ECCV)*, 2018, pp. 88–104.
- [20] G. Shim, J. Park, and I. S. Kweon, "Robust reference-based super-resolution with similarity-aware deformable convolution," in *Proceedings of the IEEE/CVF conference on computer vision and pattern recognition*, 2020, pp. 8425–8434.
- [21] J. Dai, H. Qi, Y. Xiong, Y. Li, G. Zhang, H. Hu, and Y. Wei, "Deformable convolutional networks," in *Proceedings of the IEEE international conference on computer vision*, 2017, pp. 764–773.
- [22] Y. Jiang, K. C. Chan, X. Wang, C. C. Loy, and Z. Liu, "Robust reference-based super-resolution via c2-matching," in *Proceedings of the IEEE/CVF Conference on Computer Vision and Pattern Recognition*, 2021, pp. 2103–2112.
- [23] L. Lu, W. Li, X. Tao, J. Lu, and J. Jia, "Masa-sr: Matching acceleration and spatial adaptation for reference-based image super-resolution," in *Proceedings of the IEEE/CVF Conference on Computer Vision and Pattern Recognition*, 2021, pp. 6368–6377.
- [24] A. Dosovitskiy, L. Beyer, A. Kolesnikov, D. Weissenborn, X. Zhai, T. Unterthiner, M. Dehghani, M. Minderer, G. Heigold, S. Gelly *et al.*, "An image is worth 16x16 words: Transformers for image recognition at scale," *arXiv preprint arXiv:2010.11929*, 2020.
- [25] X. Chen, C.-J. Hsieh, and B. Gong, "When vision transformers outperform resnets without pre-training or strong data augmentations," *arXiv preprint arXiv:2106.01548*, 2021.
- [26] A. Steiner, A. Kolesnikov, X. Zhai, R. Wightman, J. Uszkoreit, and L. Beyer, "How to train your vit? data, augmentation, and regularization in vision transformers," *arXiv preprint arXiv:2106.10270*, 2021.
- [27] T. Yu, G. Zhao, P. Li, and Y. Yu, "Boat: Bilateral local attention vision transformer," *arXiv preprint arXiv:2201.13027*, 2022.
- [28] W. Wang, E. Xie, X. Li, D.-P. Fan, K. Song, D. Liang, T. Lu, P. Luo, and L. Shao, "Pyramid vision transformer: A versatile backbone for dense prediction without convolutions," in *Proceedings of the IEEE/CVF International Conference on Computer Vision*, 2021, pp. 568–578.
- [29] H. Wu, B. Xiao, N. Codella, M. Liu, X. Dai, L. Yuan, and L. Zhang, "Cvt: Introducing convolutions to vision transformers," in *Proceedings of the IEEE/CVF International Conference on Computer Vision*, 2021, pp. 22–31.
- [30] K. Simonyan and A. Zisserman, "Very deep convolutional networks for large-scale image recognition," *arXiv preprint arXiv:1409.1556*, 2014.
- [31] C.-F. R. Chen, Q. Fan, and R. Panda, "Crossvit: Cross-attention multi-scale vision transformer for image classification," in *Proceedings of the IEEE/CVF international conference on computer vision*, 2021, pp. 357–366.
- [32] S. Nah, T. Hyun Kim, and K. Mu Lee, "Deep multi-scale convolutional neural network for dynamic scene deblurring," in *Proceedings of the IEEE conference on computer vision and pattern recognition*, 2017, pp. 3883–3891.
- [33] J. Sun, W. Cao, Z. Xu, and J. Ponce, "Learning a convolutional neural network for non-uniform motion blur removal," in *Proceedings of the IEEE conference on computer vision and pattern recognition*, 2015, pp. 769–777.
- [34] J. Johnson, A. Alahi, and L. Fei-Fei, "Perceptual losses for real-time style transfer and super-resolution," in *European conference on computer vision*. Springer, 2016, pp. 694–711.
- [35] IXI.[Online].<https://brain-development.org/ixi-dataset>.
- [36] J. Zbontar, F. Knoll, A. Sriram, T. Murrell, Z. Huang, M. J. Muckley, A. Defazio, R. Stern, P. Johnson, M. Bruno *et al.*, "fastMRI: An open dataset and benchmarks for accelerated MRI," *arXiv preprint arXiv:1811.08839*, 2018.
- [37] Q. Lyu, H. Shan, and G. Wang, "MRI super-resolution with ensemble learning and complementary priors," *IEEE Transactions on Computational Imaging*, vol. 6, pp. 615–624, 2020.
- [38] C.-M. Feng, Y. Yan, H. Fu, L. Chen, and Y. Xu, "Task transformer network for joint MRI reconstruction and super-resolution," in *International Conference on Medical Image Computing and Computer-Assisted Intervention*. Springer, 2021, pp. 307–317.
- [39] K. Zeng, H. Zheng, C. Cai, Y. Yang, K. Zhang, and Z. Chen, "Simultaneous single- and multi-contrast super-resolution for brain MRI images based on a convolutional neural network," *Computers in biology and medicine*, vol. 99, pp. 133–141, 2018.
- [40] B. Lim, S. Son, H. Kim, S. Nah, and K. Mu Lee, "Enhanced deep residual networks for single image super-resolution," in *Proceedings of the IEEE conference on computer vision and pattern recognition workshops*, 2017, pp. 136–144.